



Data Article

Data related to architectural bone parameters and the relationship to Ti lattice design for powder bed fusion additive manufacturing



Martine McGregor, Sagar Patel, Stewart McLachlin, Mihaela Vlasea*

University of Waterloo, Department of Mechanical and Mechatronics Engineering, Waterloo, ON N2L 3G1, Canada

ARTICLE INFO

Article history:

Received 30 September 2021

Revised 18 November 2021

Accepted 22 November 2021

Available online 26 November 2021

Keywords:

Additive manufacturing

X-ray computed tomography

Laser powder bed fusion

Lattice design

Bone replacement, Orthopaedic design

ABSTRACT

The data included in this article provides additional supporting information on our publication (McGregor et al. [1]) on the review of the natural lattice architecture in human bone and its implication towards titanium (Ti) lattice design for laser powder bed fusion and electron beam powder bed fusion. For this work, X-ray computed tomography was deployed to understand and visualize a Ti-6Al-4V lattice structure manufactured by laser powder bed fusion. This manuscript includes details about the manufacturing of the lattice structure using laser powder bed fusion and computed tomography methods used for analyzing the lattice structure. Additionally, a comprehensive literature review was conducted to understand how lattice parameters are controlled in additively manufactured Ti and Ti-alloy parts aimed at replacing or augmenting human bone. From this literature review, lattice design information was collected and is summarized in tabular form in this manuscript.

© 2021 The Author(s). Published by Elsevier Inc.





This is an open access article under the CC BY-NC-ND license (<http://creativecommons.org/licenses/by-nc-nd/4.0/>)

Abbreviations: AM, Additive manufacturing; E-PBF, Electron beam powder bed fusion; L-PBF, Laser powder bed fusion; Ti, Titanium; TPMS, Triply periodic minimal surface; XCT, X-ray computed tomography.

DOI of original article: [10.1016/j.addma.2021.102273](https://doi.org/10.1016/j.addma.2021.102273)

* Corresponding author.

E-mail address: mihaela.vlasea@uwaterloo.ca (M. Vlasea).

Social media:  (M. McGregor),  (S. Patel),  (S. McLachlin),  (M. Vlasea)

<https://doi.org/10.1016/j.dib.2021.107633>

2352-3409/© 2021 The Author(s). Published by Elsevier Inc. This is an open access article under the CC BY-NC-ND license (<http://creativecommons.org/licenses/by-nc-nd/4.0/>)

Specifications Table

Subject	Engineering, Materials science, Health, and medical sciences
Specific subject area	Additive manufacturing, Bone replacement, Metamaterials, Lattice structures, Orthopaedic design, Bone micro-architecture
Type of data	Table
How data were acquired	Instruments: Laser powder bed fusion (L-PBF) machine, X-ray computed tomography (CT) Make and model of the instruments and software used: Renishaw AM 400 (L-PBF machine), ZEISS Xradia 520 Versa (CT hardware), Dragonfly 3.0, Object Research Systems Inc. (CT software), nTopology (software)
Data format	Raw
Parameters for data collection	Analyzed
Description of data collection	The lattice sample was manufactured via laser powder bed fusion additive manufacturing and analyzed using X-ray computed tomography. The literature review on lattice design parameters for titanium alloys fabricated via powder bed fusion followed a pre-defined taxonomy and inclusion criteria. The lattice structure was manufactured using Ti-6Al-4V powder using laser powder bed fusion (L-PBF) additive manufacturing. The lattice structure was then analyzed in a 3D X-ray computed tomography (XCT) scanner. The analysis of the XCT results was performed using an image processing software. Additionally, the lattice design information presented in tabular form was collected by reviewing 49 journal articles that deployed either laser powder bed fusion (L-PBF) or electron beam powder bed fusion (E-PBF) for lattice manufacturing with the objective of replacing, repairing, or augmenting human bone.
Data source location	Multi-Scale Additive Manufacturing Laboratory, University of Waterloo, Waterloo, ON, Canada
Data accessibility	The raw and analyzed data is available with this article.
Related research article	McGregor et al. [1]

Value of the Data

- The data included in [Table 3](#) provides a comprehensive overview at attempts made at replacing and repairing human bone through Ti and Ti-6Al-4V lattice structures manufactured with powder bed fusion technologies.
- The richness of the dataset in [Table 3](#) creates value for future reference when selecting lattice design parameters to tailor structures for compressive strength, yield strength and Young's modulus in aims of matching the mechanical properties of human bone.
- The design details and the laser powder bed fusion (L-PBF) manufacturing data provided for the Voronoi lattice, a stochastic lattice structure, is important to help additive manufacturing readers reproduce the lattice structure showcased in [Figures 15 and 16](#) in [McGregor et al. \[1\]](#) using an L-PBF system. The design of the lattice structure in particular can help a reader better visualize the various surface types described in [Figure 15](#) in [McGregor et al. \[1\]](#).
- The data provided about the X-ray computed tomography (XCT) measurements and the resulting analysis results provides the additive manufacturing community and/or bone replacement interested readers with sufficient information to examine a similar lattice structure using XCT and recreate results shown in [McGregor et al. \[1\]](#).

1. Data Description

The Ti-6Al-4V Voronoi lattice structure manufactured by laser powder bed fusion (L-PBF) was analyzed in a 3D X-ray computed tomography (XCT) scanner (ZEISS Xradia 520 Versa). Voronoi lattices structures have numerous down-skin and overhanging features which cannot be controlled due to the stochastic nature of the lattice and therefore make an excellent showcase for manufacturability challenges with powder bed fusion AM. The original publication, [McGregor](#)

Table 1

X-ray computed tomography (XCT) parameters used for scanning the entire Ti-6Al-4V Voronoi lattice structure.

Parameter	Unit	Value
Voxel size	[μm]	12.54
Source power	[W]	7
Source voltage	[kV]	80
Filter	-	LE6
X-ray optic	-	0.4x lens
Source-to-sample position	[mm]	23.02
Detector-to-sample position	[mm]	103
Exposure time	[s]	1.5
Number of projections	-	2401
Binning level	-	2

Table 2

X-ray computed tomography (XCT) parameters used for scanning the high-resolution portion of the Ti-6Al-4V Voronoi lattice structure.

Parameter	Unit	Value
Voxel size	[μm]	2.00
Source power	[W]	7
Source voltage	[kV]	80
Filter	-	LE6
X-ray optic	-	4x lens
Source-to-sample position	[mm]	14.04
Detector-to-sample position	[mm]	103
Exposure time	[s]	4
Number of projections	-	3001
Binning level	-	2

et al. [1], brings into focus the manufacturability limits of the powder bed fusion technology for the Ti and Ti-alloy lattice structures intended for bone replacement and repair. Therefore, the Voronoi lattice structure was selected as the test object for demonstrating these challenges. Voronoi lattice structures are also relatively new to the AM community and not well-studied, further justifying the use of a Voronoi lattice structure in this work. The Voronoi lattice designed for comparison of manufactured versus ideal design had a design-imposed strut thickness of 500 μm , random point spacing of 50 points at 1000 μm , and $5 \times 10 \times 10$ mm in size. The design (STL) file for the Voronoi lattice structure was created in nTopology and is attached as supplementary material to this article. The important processing parameters used to obtain the XCT results for the entire lattice structure (left of Figure 15 in McGregor et al. [1]) are shown in Table 1, and the parameters used for the high resolution scan (center and right of Figure 15 in McGregor et al. [1]) are shown in Table 2. To visualize the defect space within the sample, the XCT scanned file was then analyzed using an image processing software (Dragonfly 3.0, Object Research Systems Inc., Montreal, QC) [2]. To visualize the porous defects, the XCT dataset was subjected to greyscale thresholding and segmentation into the solid material (Ti-6Al-4V) and pores. Thresholding values were manually established by examining images prior to and after thresholding to show the best contrast. Following segmentation, the resulting binarized images were used to obtain information about the aspect ratio of all the pores. Defects with aspect ratios above 0.7 were considered as rounded pores for visualization of the porous defects. The brightness, contrast, and opacity of the solid material and pores was then adjusted to highlight the pores and surface features within the XCT data volume.

The lattice design parameters dataset provided in Table 3 was collected by narrowing down to and reviewing 49 journal articles that deployed either laser powder bed fusion (L-PBF) or electron beam powder bed fusion (E-PBF) for Ti or Ti-6Al-4V lattice manufacturing with the objective of replacing, repairing, or augmenting human bone. The review methodology followed is depicted in the flowchart in Figure 1. Details about the manufacturing technology used

Table 3

Literature reporting the use of Ti lattices for the purpose of human bone replacement and/or augmentation is summarized. Lattice design parameters, lattice type, AM technology (laser powder bed fusion (L-PBF) and electron beam powder bed fusion (E-PBF)) and compressive mechanical properties were recorded, as available. Blank entries reflect data not included in the original publication. Findings from Table 3 were used to create Figures 10-14 in McGregor et al. [1].

Reference	Porosity (%)	Pore Size (μm)	Feature Thickness (μm)	Lattice Type	Unit Cell Size (mm^3)	AM Technology	Material	E (GPa)	σ_c (MPa)	σ_y (MPa)
Mobbs et al., 2017 [3]	—	—	—	FCC	—	—	Ti	—	—	—
Kim et al., 2017 [4]	—	—	—	FCC	—	E-PBF	Ti-6Al-4V	—	—	—
Choy et al., 2017 [5]	—	—	—	—	—	—	Ti	—	—	—
Phan et al., 2016 [6]	—	—	—	Simple Cubic	—	—	Ti-6Al-4V	—	—	—
Xu et al., 2016 [7]	—	—	—	—	—	E-PBF	—	—	—	—
Taniguchi et al., 2016 [8]	61.6*	309*	220.0*	Diamond	—	L-PBF	Ti	0.66*	50.0*	—
	66.4*	632*	416.0*	Diamond	—	L-PBF	Ti	0.56*	50.0*	—
	64.0*	956*	577.0*	Diamond	—	L-PBF	Ti	0.76*	16.0*	—
de Wild et al., 2013 [9]	83.0	550*	200.0	Simple Cubic	—	L-PBF	Ti	0.76*	16.0*	—
Hilton et al., 2017 [10]	—	—	—	—	—	E-PBF	Ti-6Al-4V	—	—	—
Schouman et al., 2016 [11]	53.0	800-1500	—	—	—	L-PBF	Ti	37.90	—	—
Arabnejad et al., 2017 [12]	70.0	500	200.0	Tetrahedron	—	L-PBF	Ti-6Al-4V	—	—	—
Wu et al., 2013 [13]	68.0	710	—	—	—	E-PBF	Ti-6Al-4V	2.50	63.0	—
Biamond et al., 2013 [14]	63.0	250-800	—	—	—	L-PBF	Ti	—	—	—
	49.0	350-1400	—	—	—	E-PBF	Ti	—	—	—
Xue et al., 2007 [15]	17.0	100	—	—	—	L-PBF	Ti	44.00	463.0	—
	20.0	300	—	—	—	L-PBF	Ti	42.00	444.0	—
	27.0	450	—	—	—	L-PBF	Ti	24.30	205.0	—
	48.0	550	—	—	—	L-PBF	Ti	7.70	54.0	—
	58.0	800	—	—	—	L-PBF	Ti	2.60	24.0	—
Van der Stok et al., 2013 [16]	88.0	—	120.0	Dodecahedron	—	L-PBF	Ti-230	14.30	77.7	—
	68.0	—	230.0	Dodecahedron	—	L-PBF	Ti-120	0.38	1.6	—
Srivas et al., 2017 [17]	58.0	500	348.0	Simple Cubic	—	FDM	Ti-6Al-4V	0.45	39.6	—
Wieding et al., 2015 [18]	70.0	700	400.0	Simple Cubic	1.33	L-PBF	Ti-6Al-4V	8.22	168.2	—
Van Bael et al., 2012 [19]	—	500-1000	200.0	Triangular	—	L-PBF	Ti-6Al-4V	—	—	—
	—	500-1000	200.0	Honeycomb	—	—	—	—	—	—
	—	500-1000	200.0	Hexagonal	—	—	Ti-6Al-4V	—	—	—
	—	500-1000	200.0	Honeycomb	—	—	—	—	—	—
	—	500-1000	200.0	Rectangular honeycomb	—	—	Ti-6Al-4V	—	—	—

(continued on next page)

Table 3 (continued)

Reference	Porosity (%)	Pore Size (μm)	Feature Thickness (μm)	Lattice Type	Unit Cell Size (mm^3)	AM Technology	Material	E (GPa)	σ_c (MPa)	σ_y (MPa)
Otsuki et al., 2006 [20]	48.0	233*	—	Porous foam	—	—	Ti	—	—	—
	50.0	303*	—	Porous foam	—	—	Ti	—	—	—
	69.0	268*	—	Porous foam	—	—	Ti	—	—	—
	70.0	333*	—	Porous foam	—	—	Ti	—	—	—
Ghouse et al., 2019 [21]	87.3	830	210.0	Stochastic	—	L-PBF	Ti	1.70	550.0	—
Zhao et al., 2018 [22]	67.0	500	—	Tetrahedron	—	L-PBF	Ti	4.66	417.7	135.6
	84.0	1000	—	Tetrahedron	—	L-PBF	Ti	1.31	100.7	31.8
	63.0	500	—	Octahedron	—	L-PBF	Ti	5.51	453.0	228.4
	77.0	1000	—	Octahedron	—	L-PBF	Ti	2.57	117.3	81.2
Fousova et al., 2017 [23]	48.4	—	300.0	Rhombic	2	L-PBF	Ti-6Al-4V	47.60	422.0	—
	62.1	—	300.0	Dodecahedron Rhombic	2	L-PBF	Ti-6Al-4V	30.50	257.0	—
	79.2	—	300.0	Rhombic Dodecahedron	2	L-PBF	Ti-6Al-4V	—	19.0	—
Arabnejad et al., 2016 [24]	50.0	500	390.0	Tetrahedron	1.52	L-PBF	Ti	4.30	219.0	—
	60.0	500	310.0	Tetrahedron	1.39	L-PBF	Ti	3.00	136.0	—
	70.0	500	240.0	Tetrahedron	1.27	L-PBF	Ti	2.80	120.0	—
	75.0	500	200.0	Tetrahedron	1.2	L-PBF	Ti	2.00	68.0	—
	50.0	770	400.0	Octahedron	1.66	L-PBF	Ti	4.50	228.0	—
	60.0	770	320.0	Octahedron	1.54	L-PBF	Ti	3.40	145.0	—
	70.0	770	250.0	Octahedron	1.44	L-PBF	Ti	1.40	31.0	—
	75.0	770	200.0	Octahedron	1.37	L-PBF	Ti	1.30	39.0	—
Moiduddin et al., 2017 [25]	49.8	700	800.0	BCC	2	E-PBF	Ti-6Al-4V	1.20	62.0	—

(continued on next page)

Table 3 (continued)

Reference	Porosity (%)	Pore Size (μm)	Feature Thickness (μm)	Lattice Type	Unit Cell Size (mm^3)	AM Technology	Material	E (GPa)	σ_c (MPa)	σ_y (MPa)
Harrysson et al., 2008 [26]	59.0	—	—	Rhombic Dodecahedron	3	E-PBF	Ti-6Al-4V	—	91.7	—
	59.0	—	—	Rhombic Dodecahedron	3	E-PBF	Ti-6Al-4V	—	94.1	—
	59.0	—	—	Rhombic Dodecahedron	3	E-PBF	Ti-6Al-4V	—	94.9	—
	92.0	—	—	Rhombic Dodecahedron	8	E-PBF	Ti-6Al-4V	—	2.9	—
	92.0	—	—	Rhombic Dodecahedron	8	E-PBF	Ti-6Al-4V	—	3.1	—
Wong et al., 2015 [27]	95.0	—	—	—	10	—	—	—	0.8	—
Taheri et al., 2016 [28]	70.0	720	350.0	—	—	L-PBF	Ti-6Al-4V	—	—	—
	20.0	—	800.0	—	2	L-PBF	NiTi	47.00	72.0	—
	32.0	—	700.0	—	2	L-PBF	NiTi	41.20	55.0	—
	45.0	—	600.0	—	2	L-PBF	NiTi	30.00	39.0	—
	58.0	—	500.0	—	2	L-PBF	NiTi	20.50	23.0	—
Wang et al., 2017 [29]	71.0	—	400.0	—	2	L-PBF	NiTi	10.00	15.0	—
	72.3	—	400.0	BCC	2	L-PBF	Ti-6Al-4V	3.40	—	184.4
	56.3	—	600.0	BCC	2	L-PBF	Ti-6Al-4V	4.80	—	333.0
	29.3	—	900.0	BCC	2	L-PBF	Ti-6Al-4V	10.40	—	842.6
Marin et al., 2013 [30]	66.3*	660*	—	Hexagonal Honeycomb	2	E-PBF	Ti	0.23*	15.5*	—
	75.5*	1370*	—	Hexagonal Honeycomb	2	E-PBF	Ti	0.04*	5.3*	—
Lin et al., 2013 [31]	—	—	—	—	—	L-PBF	Ti-6Al-4V	35.00	—	—
Barbas et al., 2012 [32]	53.0	1180	—	Custom	—	L-PBF	Ti	28.00	180.0	—
Wieding et al., 2014 [33]	—	799	416.0	Simple Cubic	1.215	L-PBF	Ti-6Al-4V	15.00	—	—
	—	797	1448.0	FCC	4.024	L-PBF	Ti-6Al-4V	15.00	—	—
	—	789	393.0	Custom	1.182	L-PBF	Ti-6Al-4V	15.00	—	—
du Pleiss et al., 2018 [34]	50.0	—	1317.0	Fluorite	5	L-PBF	Ti-6Al-4V	3.80	200.0	—
	50.0	—	1669.0	BCC	5	L-PBF	Ti-6Al-4V	3.60	200.0	—
Arjunan et al., 2020 [35]	71.0	—	—	Custom	—	L-PBF	Ti-6Al-4V	6.81	198.5	125.9
	74.3	—	—	Custom	—	L-PBF	Ti-6Al-4V	5.14	195.0	79.5
	81.2	—	—	Custom	—	L-PBF	Ti-6Al-4V	2.58	77.4	67.1
	83.0	—	—	Custom	—	L-PBF	Ti-6Al-4V	10.90	284.5	236.3
	83.1	—	—	Custom	—	L-PBF	Ti-6Al-4V	3.69	69.1	59.0
	91.4	—	—	Custom	—	L-PBF	Ti-6Al-4V	2.21	45.0	39.5

(continued on next page)

Table 3 (continued)

Reference	Porosity (%)	Pore Size (μm)	Feature Thickness (μm)	Lattice Type	Unit Cell Size (mm^3)	AM Technology	Material	E (GPa)	σ_c (MPa)	σ_y (MPa)
Murr et al., 2011 [36]	—	—	200.0	Dodecahedron	—	E-PBF	Ti-6Al-4V	—	—	—
	—	—	—	Stochastic	—	E-PBF	Ti-6Al-4V	—	—	—
Soro et al., 2019 [37]	25*	138*	768*	Schwarz TPMS	—	L-PBF	Ti-6Al-4V	58*	—	520*
	42*	282*	635*	Schwarz TPMS	—	L-PBF	Ti-6Al-4V	44*	—	325*
	64*	596	552*	Schwarz TPMS	—	L-PBF	Ti-6Al-4V	22.3*	—	160*
Alabort et al., 2019 [38]	85.0	500	—	Diamond TPMS	1	L-PBF	Ti-6Al-4V	0.57	65.0	—
	85.0	350	—	Neovious TPMS	1	L-PBF	Ti-6Al-4V	0.90	50.0	—
	85.0	200	—	Gyroid TPMS	1	L-PBF	Ti-6Al-4V	1.30	55.0	—
Zhang et al., 2018 [39]	79.5	650	200.0	Diamond	—	L-PBF	Ti-6Al-4V	1.22	36.5	—
	76.3	650	250.0	Diamond	—	L-PBF	Ti-6Al-4V	2.00	56.6	—
	72.6	650	300.0	Diamond	—	L-PBF	Ti-6Al-4V	3.02	85.8	—
	67.9	650	350.0	Diamond	—	L-PBF	Ti-6Al-4V	3.79	109.2	—
	66.1	650	400.0	Diamond	—	L-PBF	Ti-6Al-4V	5.15	144.9	—
Bartolomeu et al., 2021 [40]	64.2	500	300.0	Simple Cubic	0.8	L-PBF	Ti-6Al-4V	42.00	—	—
	70.3	600	300.0	Simple Cubic	0.9	L-PBF	Ti-6Al-4V	28.60	—	—
	84.0	500	150.0	Simple Cubic	0.65	L-PBF	Ti-6Al-4V	22.60	—	—
	87.6	600	150.0	Simple Cubic	0.75	L-PBF	Ti-6Al-4V	16.10	—	—
	93.3	600	100.0	Simple Cubic	0.7	L-PBF	Ti-6Al-4V	12.40	—	—
Balci et al., 2021 [41]	54.5	540	0.3	Custom	—	L-PBF	Ti-6Al-4V	—	—	—
	54.1	890	0.4	Custom	—	L-PBF	Ti-6Al-4V	—	—	—
	61.0	130	0.6	Custom	—	L-PBF	Ti-6Al-4V	—	—	—
	39.3	390	0.2	Custom	—	L-PBF	Ti-6Al-4V	—	—	—
	48.9	620	0.3	Custom	—	L-PBF	Ti-6Al-4V	—	—	—
	60.6	650	0.3	Custom	—	L-PBF	Ti-6Al-4V	—	—	—
Xiong et al., 2020 [42]	65.8	631	283.0	Diamond	—	L-PBF	Ti-6Al-4V	4.72	170.5	126.8
	67.1	643	285.0	Hexagonal	—	L-PBF	Ti-6Al-4V	3.79	163.0	110.9
	51.4	636	283.0	Honeycomb	—	L-PBF	Ti-6Al-4V	10.07	419.8	350.1
	52.7	643	285.0	Hexagonal	—	L-PBF	Ti-6Al-4V	10.99	536.9	423.8
	—	—	—	Honeycomb	—	L-PBF	Ti-6Al-4V	—	—	—
Dallago et al., 2021 [43]	92.7	—	670.0	Simple Cubic	4	L-PBF	Ti-6Al-4V	3.02	16.0	16.0
	92.7	—	670.0	Simple Cubic	4	L-PBF	Ti-6Al-4V	1.75	9.0	9.0
	94.1	—	670.0	Simple Cubic	4	L-PBF	Ti-6Al-4V	1.84	9.0	9.0
	92.7	—	500.0	Simple Cubic	3	L-PBF	Ti-6Al-4V	2.98	14.0	15.0
Bari & Arjunan, 2019 [44]	63.6	—	—	Custom	—	L-PBF	Ti-6Al-4V	13.87	—	—
	56.9	—	—	Custom	—	L-PBF	Ti-6Al-4V	19.52	—	—
	68.0	—	—	Custom	—	L-PBF	Ti-6Al-4V	10.74	—	—
	74.0	—	100.0	Custom	—	L-PBF	Ti-6Al-4V	5.09	169.0	—
	61.0	—	500.0	Custom	—	L-PBF	Ti-6Al-4V	6.07	342.0	—
	55.0	—	900.0	Custom	—	L-PBF	Ti-6Al-4V	5.42	280.0	—









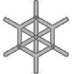





















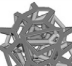
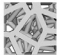
(continued on next page)

Table 3 (continued)

Reference	Porosity (%)	Pore Size (μm)	Feature Thickness (μm)	Lattice Type	Unit Cell Size (mm^3)	AM Technology	Material	E (GPa)	σ_c (MPa)	σ_y (MPa)	
Heinl et al., 2008 [45]	81.1	1230	—	Diamond	—	E-PBF	Ti-6Al-4V	1.60	29.3	22.0	
	80.8	1230	—	Diamond	—	E-PBF	Ti-6Al-4V	0.90	21.0	16.1	
	59.5	450	—	Simple Cubic	—	E-PBF	Ti-6Al-4V	12.90	148.4	107.5	
	59.5	450	—	Simple Cubic	—	E-PBF	Ti-6Al-4V	3.90	127.1	49.6	
Liu et al., 2018 [46]	97.0	—	—	Diamond	5.5	L-PBF	Ti-6Al-4V	0.34	2.0	—	
	81.0	—	—	Diamond	5.5	L-PBF	Ti-6Al-4V	1.40	78.0	—	
Yan et al., 2015 [47]	80.0	1600*	—	Gyroid TPMS	—	L-PBF	Ti-6Al-4V	1.25*	81.3*	—	
	95.0	560*	—	Gyroid TPMS	—	L-PBF	Ti-6Al-4V	0.13*	6.5*	—	
	80.0	1450*	—	Diamond TPMS	—	L-PBF	Ti-6Al-4V	1.25*	69.2*	—	
	95.0	480*	—	Diamond TPMS	—	L-PBF	Ti-6Al-4V	0.12*	4.7*	—	
Ge et al., 2020 [48]	72.6	550	—	Trabecular	—	L-PBF	Ti-6Al-4V	5.58	55.7	—	
	70.0	550	—	Gyroid TPMS	—	L-PBF	Ti-6Al-4V	5.51	34.6	—	
El-Sayed et al., 2020 [49]	82.4	—	840.0	Diamond	—	L-PBF	Ti-6Al-4V	0.35	19.3	—	
	78.1	—	600.0	Diamond	—	L-PBF	Ti-6Al-4V	0.44	26.1	—	
	26.4	—	360.0	Diamond	—	L-PBF	Ti-6Al-4V	9.59	150.0	—	
	93.2	—	360.0	Diamond	—	L-PBF	Ti-6Al-4V	0.05	3.7	—	
	65.5	—	600.0	Diamond	—	L-PBF	Ti-6Al-4V	7.73	184.5	—	
	73.1	—	840.0	Diamond	—	L-PBF	Ti-6Al-4V	1.55	82.4	—	
	75.0	—	600.0	Diamond	—	L-PBF	Ti-6Al-4V	1.28	47.3	—	
	89.4	—	200.0	Diamond	—	L-PBF	Ti-6Al-4V	0.22	10.2	—	
	43.9	—	360.0	Diamond	—	L-PBF	Ti-6Al-4V	4.95	145.8	—	
	64.5	—	840.0	Diamond	—	L-PBF	Ti-6Al-4V	4.19	68.7	—	
	90.3	—	600.0	Diamond	—	L-PBF	Ti-6Al-4V	0.16	7.5	—	
	90.8	—	360.0	Diamond	—	L-PBF	Ti-6Al-4V	0.26	8.8	—	
	20.0	—	600.0	Diamond	—	L-PBF	Ti-6Al-4V	11.83	200.0	—	
	51.4	—	840.0	Diamond	—	L-PBF	Ti-6Al-4V	9.31	95.5	—	
	55.5	—	1000.0	Diamond	—	L-PBF	Ti-6Al-4V	8.34	228.4	—	
	74.8	—	600.0	Diamond	—	L-PBF	Ti-6Al-4V	1.41	52.2	—	
	76.0	—	600.0	Diamond	—	L-PBF	Ti-6Al-4V	1.17	49.3	—	
	Wang et al., 2020 [50]	64.4	—	670.0	—	3	E-PBF	Ti-6Al-4V	14.70	169.7	—
		62.4	—	500.0	—	4	E-PBF	Ti-6Al-4V	21.00	169.5	—
		59.7	—	400.0	—	5	E-PBF	Ti-6Al-4V	20.00	229.0	—
59.9		—	670.0	—	3	E-PBF	Ti-6Al-4V	18.30	229.1	—	
58.2		—	500.0	—	4	E-PBF	Ti-6Al-4V	23.30	243.9	—	
58.3		—	400.0	—	5	E-PBF	Ti-6Al-4V	25.30	250.7	—	
Zhang et al., 2020 [51]		—	—	—	Gyroid TPMS	Graded	L-PBF	Ti-6Al-4V	—	—	—

Table 4

A glossary of the lattice types described in Table 3 has been included. The unit cells are $10 \times 10 \times 10$ mm with a feature thickness of 1mm. The glossary includes an isometric and frontal view of each unit cell with a bounding box.

Lattice name	Isometric view	Front view	References
Body Centered Cubic (BCC)			[25], [29], [34]
Face Centered Cubic (FCC)			[3], [4], [33]
Simple Cubic			[5], [9], [17], [18], [33], [40], [43], [45]
Diamond			[8], [39], [42], [45], [46], [49]
Fluorite			[34]
Hexagonal Honeycomb			[19], [30], [42]
Triangular Honeycomb			[19]
Rectangular Honeycomb			[19]
Tetrahedron			[12], [22], [24]
Octahedron			[22], [24]
Dodecahedron			[16], [23], [26], [36]
Schwarz TPMS			[37]
Gyroid TPMS			[38], [47], [51]
Diamond TPMS			[38], [47]
Neovious TPMS			[38]
Stochastic (e.g., Voronoi)			[20], [21], [36]
Custom	Varies	Varies	[32], [33], [35], [41], [44]

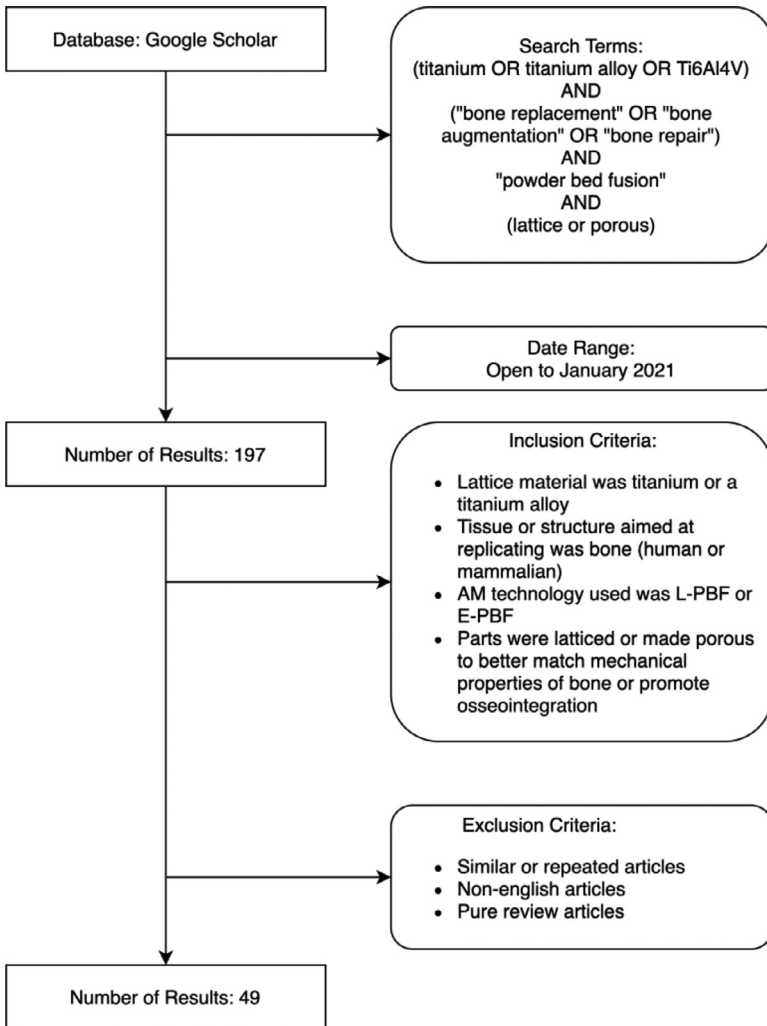


Fig. 1. A flowchart has been utilized to describe the review methodology with the search terms, inclusion and exclusion criteria outlined.

(L-PBF or E-PBF), lattice type, lattice porosity (%), lattice pore size (μm), lattice feature thickness (μm), material (Ti or Ti-6Al-4V), Young's modulus (E , GPa), compressive yield strength (σ_y), and ultimate compressive strength (σ_u , MPa) are provided in Table 3. The values reported in Table 3 represent those values reported in each individual study, which differ from individual lattice properties to average compressive mechanical properties from multiple tests. Individual values were included whenever available, averages from large data sets are denoted with a "*", and data not reported in a given study was denoted "-". The addition of these characters is aimed at improving data interpretation and allowing readers to use the table to appropriately design Ti lattice for bone replacement and repair in the future, or to build upon this literature. Findings from Table 3 were used to create Figures 10-14 in McGregor et al. [1].

2. Experimental Design, Materials and Methods

The Voronoi lattice structure was manufactured using Ti-6Al-4V powder on the reduced build volume (RBV) of a modulated laser powder bed fusion (L-PBF) system (AM 400, Renishaw, UK). The design (STL) file for the Voronoi lattice structure is attached as supplementary material to this article. The powder used was plasma atomized, grade 23 with a size distribution of 15–45 μm (d10 of 20 μm , d50 of 34 μm , and d90 of 44 μm), provided by AP&C (Quebec, Canada). For the AM 400 system, the beam spot radius at the focal point is given by $r_B = 35 \mu\text{m}$ (beam spot diameter = 70 μm), which was kept constant for this study. The scan strategy followed this order: scanning of the core using the meander scanning strategy, followed by a single border scan that involves melting of the edge of each contour within a layer specified by the CAD of the lattice structure. The important core process parameters used for manufacturing the Voronoi include a laser power of 135 W, point distance of 55 μm , exposure time of 45 μs , a powder layer thickness value of 30 μm , and a hatching distance of 70 μm . For the border scanning, a laser power of 200 W, point distance of 45 μm , exposure time of 70 μs were used. The build plate was kept at room temperature for the print, and the oxygen level was set to 500 ppm. Argon was the shielding gas used for the printing process. The lattice structure was printed directly on the build plate and was removed from the build plate using electro-discharge machining (EDM).

Ethics Statement

The authors declare that this submission follows the ethical requirements for publication in Data in Brief.

Declaration of Competing Interest

The authors wish to declare that there are no conflicts of interest.

CRedit Author Statement

Martine McGregor: Conceptualization, Methodology, Investigation, Formal analysis, Data curation, Writing – original draft, Writing – review & editing, Visualization; **Sagar Patel:** Methodology, Investigation, Formal analysis, Software, Writing – original draft, Writing – review & editing, Visualization; **Stewart McLachlin:** Conceptualization, Methodology, Writing – review & editing, Supervision, Project administration; **Mihaela Vlasea:** Conceptualization, Methodology, Writing – review & editing, Supervision, Project administration, Funding acquisition.

Acknowledgments

Sagar Patel and Mihaela Vlasea appreciate the funding support received from Federal Economic Development Agency for Southern Ontario (FedDev Ontario grant number 814654). Additionally, Sagar Patel and Mihaela Vlasea would like to acknowledge the help of Jerry Rathapakdee and Henry Ma with the deployment and characterization of the laser powder bed fusion builds. Martine McGregor is supported by the Natural Sciences and Engineering Research Council of Canada doctoral scholarship. The authors would like to thank nTopology, Inc. for supporting us with a license to their software for use in the design process.

Supplementary Materials

Supplementary material associated with this article can be found in the online version at doi:[10.1016/j.dib.2021.107633](https://doi.org/10.1016/j.dib.2021.107633).

References

- [1] M. McGregor, S. Patel, S. McLachlin, M. Vlasea, Architectural Bone Parameters and the Relationship to Titanium Lattice Design for Powder Bed Fusion Additive Manufacturing, Additive Manufacturing, 2021.
- [2] Dragonfly 3D visualization and analysis solutions for scientific and industrial data, (n.d.). <https://www.theobjects.com/dragonfly/> (accessed December 18, 2020).
- [3] R.J. Mobbs, M. Coughlan, R. Thompson, C.E. Sutterlin, K. Phan, The utility of 3D printing for surgical planning and patient-specific implant design for complex spinal pathologies: case report. *J. Neurosurgery: Spine* 26 (2017) 513–518.
- [4] D. Kim, J.-Y. Lim, K.-W. Shim, J.W. Han, S. Yi, D.H. Yoon, K.N. Kim, Y. Ha, G.Y. Ji, D.A. Shin, Sacral reconstruction with a 3D-printed implant after hemisacrectomy in a patient with sacral osteosarcoma: 1-year follow-up result, *Yonsei Med. J.* 58 (2017) 453.
- [5] W.J. Choy, R.J. Mobbs, B. Wilcox, S. Phan, K. Phan, C.E. Sutterlin III, Reconstruction of thoracic spine using a personalized 3D-printed vertebral body in adolescent with T9 primary bone tumor, *World Neurosurg.* 105 (2017) 1032–e13.
- [6] K. Phan, A. Sgro, M.M. Maharaj, P. D'Urso, R.J. Mobbs, Application of a 3D custom printed patient specific spinal implant for C1/2 arthrodesis, *J. Spine Surg.* 2 (2016) 314.
- [7] N. Xu, F. Wei, X. Liu, L. Jiang, H. Cai, Z. Li, M. Yu, F. Wu, Z. Liu, Reconstruction of the upper cervical spine using a personalized 3D-printed vertebral body in an adolescent with Ewing sarcoma, *Spine* 41 (2016) E50–E54.
- [8] N. Taniguchi, S. Fujibayashi, M. Takemoto, K. Sasaki, B. Otsuki, T. Nakamura, T. Matsushita, T. Kokubo, S. Matsuda, Effect of pore size on bone ingrowth into porous titanium implants fabricated by additive manufacturing: an in vivo experiment, *Mater. Sci. Eng.: C* 59 (2016) 690–701.
- [9] M. de Wild, R. Schumacher, K. Mayer, E. Schkommodau, D. Thoma, M. Bredell, A. Kruse Gujer, K.W. Grätz, F.E. Weber, Bone regeneration by the osteoconductivity of porous titanium implants manufactured by selective laser melting: a histological and micro computed tomography study in the rabbit, *Tissue Eng. Part A* 19 (2013) 2645–2654.
- [10] T.L. Hilton, N. Campbell, K. Hosking, Additive manufacturing in orthopaedics: clinical implications, *SA Orthopaedic J.* 16 (2017) 63–67.
- [11] T. Schouman, M. Schmitt, C. Adam, G. Dubois, P. Rouch, Influence of the overall stiffness of a load-bearing porous titanium implant on bone ingrowth in critical-size mandibular bone defects in sheep, *J. Mech. Behav. Biomed. Mater.* 59 (2016) 484–496.
- [12] S. Arabnejad, B. Johnston, M. Tanzer, D. Pasini, Fully porous 3D printed titanium femoral stem to reduce stress-shielding following total hip arthroplasty, *J. Orthop. Res.* 35 (2017) 1774–1783.
- [13] S.-H. Wu, Y. Li, Y.-Q. Zhang, X.-K. Li, C.-F. Yuan, Y.-L. Hao, Z.-Y. Zhang, Z. Guo, Porous titanium-6 aluminum-4 vanadium cage has better osseointegration and less micromotion than a poly-ether-ether-ketone cage in sheep vertebral fusion, *Artif. Organs* 37 (2013) E191–E201.
- [14] J.E. Biemond, G. Hannink, N. Verdonschot, P. Buma, Bone ingrowth potential of electron beam and selective laser melting produced trabecular-like implant surfaces with and without a biomimetic coating, *J. Mater. Sci. Mater. Med.* 24 (2013) 745–753.
- [15] W. Xue, B.V. Krishna, A. Bandyopadhyay, S. Bose, Processing and biocompatibility evaluation of laser processed porous titanium, *Acta Biomater.* 3 (2007) 1007–1018.
- [16] J. der Stok, O.P. der Jagt, S. Amin Yavari, M.F.P. De Haas, J.H. Waarsing, H. Jahr, E.M.M. Van Lieshout, P. Patka, J.A.N. Verhaar, A.A. Zadpoor, others, Selective laser melting-produced porous titanium scaffolds regenerate bone in critical size cortical bone defects, *J. Orthop. Res.* 31 (2013) 792–799.
- [17] P.K. Srivas, K. Kapat, P. Dadhich, P. Pal, J. Dutta, P. Datta, S. Dhara, Osseointegration assessment of extrusion printed Ti6Al4V scaffold towards accelerated skeletal defect healing via tissue in-growth, *Bioprinting* 6 (2017) 8–17.
- [18] J. Wieding, T. Lindner, P. Bergschmidt, R. Bader, Biomechanical stability of novel mechanically adapted open-porous titanium scaffolds in metatarsal bone defects of sheep, *Biomaterials* 46 (2015) 35–47.
- [19] S. Van Bael, Y.C. Chai, S. Truscello, M. Moesen, G. Kerckhofs, H. Van Oosterwyck, J.-P. Kruth, J. Schrooten, The effect of pore geometry on the in vitro biological behavior of human periosteum-derived cells seeded on selective laser-melted Ti6Al4V bone scaffolds, *Acta Biomater.* 8 (2012) 2824–2834.
- [20] B. Otsuki, M. Takemoto, S. Fujibayashi, M. Neo, T. Kokubo, T. Nakamura, Pore throat size and connectivity determine bone and tissue ingrowth into porous implants: three-dimensional micro-CT based structural analyses of porous bioactive titanium implants, *Biomaterials* 27 (2006) 5892–5900.
- [21] S. Ghose, N. Reznikov, O.R. Boughton, S. Babu, K.C.G. Ng, G. Blunn, J.P. Cobb, M.M. Stevens, J.R.T. Jeffers, The design and in vivo testing of a locally stiffness-matched porous scaffold, *Appl. Mater. Today* 15 (2019) 377–388, doi:10.1016/j.apmt.2019.02.017.
- [22] D. Zhao, Y. Huang, Y. Ao, C. Han, Q. Wang, Y. Li, J. Liu, Q. Wei, Z. Zhang, Effect of pore geometry on the fatigue properties and cell affinity of porous titanium scaffolds fabricated by selective laser melting, *J. Mech. Behav. Biomed. Mater.* 88 (2018) 478–487.
- [23] M. Fousová, D. Vojtěch, J. Kubásek, E. Jablonská, J. Fojt, Promising characteristics of gradient porosity Ti-6Al-4V alloy prepared by SLM process, *J. Mech. Behav. Biomed. Mater.* 69 (2017) 368–376.
- [24] S. Arabnejad, R.B. Johnston, J.A. Pura, B. Singh, M. Tanzer, D. Pasini, High-strength porous biomaterials for bone replacement: a strategy to assess the interplay between cell morphology, mechanical properties, bone ingrowth and manufacturing constraints, *Acta Biomater.* 30 (2016) 345–356.

- [25] K. Moiduddin, S. Darwish, A. Al-Ahmari, S. ElWatidy, A. Mohammad, W. Ameen, Structural and mechanical characterization of custom design cranial implant created using additive manufacturing, *Electron. J. Biotechnol.* 29 (2017) 22–31.
- [26] O.L.A. Harrysson, O. Cansizoglu, D.J. Marcellin-Little, D.R. Cormier, H.A. West II, Direct metal fabrication of titanium implants with tailored materials and mechanical properties using electron beam melting technology, *Mater. Sci. Eng.: C* 28 (2008) 366–373.
- [27] K.C. Wong, S.M. Kumta, N.V. Geel, J. Demol, One-step reconstruction with a 3D-printed, biomechanically evaluated custom implant after complex pelvic tumor resection, *Comput. Aided Surg.* 20 (2015) 14–23.
- [28] M. Taheri Andani, C. Haberland, J.M. Walker, M. Karamooz, A. Sadi Turabi, S. Saedi, R. Rahmanian, H. Karaca, D. Dean, M. Kadhodaei, others, Achieving biocompatible stiffness in NiTi through additive manufacturing, *J. Intell. Mater. Syst. Struct.* 27 (2016) 2661–2671.
- [29] L. Wang, J. Kang, C. Sun, D. Li, Y. Cao, Z. Jin, Mapping porous microstructures to yield desired mechanical properties for application in 3D printed bone scaffolds and orthopaedic implants, *Mater. Design* 133 (2017) 62–68.
- [30] E. Marin, M. Pressacco, S. Fusi, A. Lanzutti, S. Turchet, L. Fedrizzi, Characterization of grade 2 commercially pure trabecular titanium structures, *Mater. Sci. Eng.: C* 33 (2013) 2648–2656.
- [31] W.-S. Lin, T.L. Starr, B.T. Harris, A. Zandinejad, D. Morton, Additive manufacturing technology (direct metal laser sintering) as a novel approach to fabricate functionally graded titanium implants: preliminary investigation of fabrication parameters, *The Int. J. Oral Maxillofacial Implants* 28 (2013) 1490–1495.
- [32] A. Barbas, A.-S. Bonnet, P. Lipinski, R. Pesci, G. Dubois, Development and mechanical characterization of porous titanium bone substitutes, *J. Mech. Behav. Biomed. Mater.* 9 (2012) 34–44.
- [33] J. Wieding, A. Wolf, R. Bader, Numerical optimization of open-porous bone scaffold structures to match the elastic properties of human cortical bone, *J. Mech. Behav. Biomed. Mater.* 37 (2014) 56–68.
- [34] A. du Plessis, I. Yadroitsava, I. Yadroitsev, Ti6Al4V lightweight lattice structures manufactured by laser powder bed fusion for load-bearing applications, *Optics Laser Technol.* 108 (2018) 521–528.
- [35] A. Arjunan, M. Demetriou, A. Baroutaji, C. Wang, Mechanical performance of highly permeable laser melted Ti6Al4V bone scaffolds, *J. Mech. Behav. Biomed. Mater.* 102 (2020) 103517.
- [36] L.E. Murr, K.N. Amato, S.J. Li, Y.X. Tian, X.Y. Cheng, S.M. Gaytan, E. Martinez, P.W. Shindo, F. Medina, R.B. Wicker, Microstructure and mechanical properties of open-cellular biomaterials prototypes for total knee replacement implants fabricated by electron beam melting, *J. Mech. Behav. Biomed. Mater.* 4 (2011) 1396–1411.
- [37] N. Soro, H. Attar, X. Wu, M.S. Dargusch, Investigation of the structure and mechanical properties of additively manufactured Ti-6Al-4V biomedical scaffolds designed with a Schwartz primitive unit-cell, *Mater. Sci. Eng.: A* 745 (2019) 195–202.
- [38] E. Alabort, D. Barba, R.C. Reed, Design of metallic bone by additive manufacturing, *Scr. Mater.* 164 (2019) 110–114.
- [39] B. Zhang, X. Pei, C. Zhou, Y. Fan, Q. Jiang, A. Ronca, U. D'Amora, Y. Chen, H. Li, Y. Sun, others, The biomimetic design and 3D printing of customized mechanical properties porous Ti6Al4V scaffold for load-bearing bone reconstruction, *Mater. Design* 152 (2018) 30–39.
- [40] F. Bartolomeu, M.M. Costa, N. Alves, G. Miranda, F.S. Silva, Selective Laser Melting of Ti6Al4V sub-millimetric cellular structures: prediction of dimensional deviations and mechanical performance, *J. Mech. Behav. Biomed. Mater.* 113 (2021) 104123.
- [41] A. Balci, F. Kucukaltun, M.F. Aycan, Y. Usta, T. Demir, Reproducibility of Replicated Trabecular Bone Structures from Ti6Al4V Extralox Interstitials Powder by Selective Laser Melting, *Arabian Journal for Science and Engineering* 46 (2021) 2527–2541.
- [42] Y.-Z. Xiong, R.-N. Gao, H. Zhang, L.-L. Dong, J.-T. Li, X. Li, Rationally designed functionally graded porous Ti6Al4V scaffolds with high strength and toughness built via selective laser melting for load-bearing orthopedic applications, *J. Mech. Behav. Biomed. Mater.* 104 (2020) 103673.
- [43] M. Dallago, S. Raghavendra, V. Luchin, G. Zappini, D. Pasini, M. Benedetti, The role of node fillet, unit-cell size and strut orientation on the fatigue strength of Ti-6Al-4V lattice materials additively manufactured via laser powder bed fusion, *Int. J. Fatigue* 142 (2021) 105946.
- [44] K. Bari, A. Arjunan, Extra low interstitial titanium based fully porous morphological bone scaffolds manufactured using selective laser melting, *J. Mech. Behav. Biomed. Mater.* 95 (2019) 1–12.
- [45] P. Heintl, L. Müller, C. Körner, R.F. Singer, F.A. Müller, Cellular Ti-6Al-4V structures with interconnected macro porosity for bone implants fabricated by selective electron beam melting, *Acta Biomater.* 4 (2008) 1536–1544.
- [46] F. Liu, D.Z. Zhang, P. Zhang, M. Zhao, S. Jafar, Mechanical properties of optimized diamond lattice structure for bone scaffolds fabricated via selective laser melting, *Materials* 11 (2018) 374.
- [47] C. Yan, L. Hao, A. Hussein, P. Young, Ti-6Al-4V triply periodic minimal surface structures for bone implants fabricated via selective laser melting, *J. Mech. Behav. Biomed. Mater.* 51 (2015) 61–73.
- [48] J. Ge, J. Huang, Y. Lei, P. O'Reilly, M. Ahmed, C. Zhang, X. Yan, S. Yin, Microstructural features and compressive properties of SLM Ti6Al4V lattice structures, *Surf. Coat. Technol.* 403 (2020) 126419.
- [49] M.A. El-Sayed, K. Essa, M. Ghazy, H. Hassanin, Design optimization of additively manufactured titanium lattice structures for biomedical implants, *The Int. J. Adv. Manuf. Technol.* 110 (2020) 2257–2268.
- [50] P. Wang, X. Li, Y. Jiang, M.L.S. Nai, J. Ding, J. Wei, Electron beam melted heterogeneously porous microlattices for metallic bone applications: design and investigations of boundary and edge effects, *Additive Manuf.* 36 (2020) 101566.
- [51] X.-Y. Zhang, X.-C. Yan, G. Fang, M. Liu, Biomechanical influence of structural variation strategies on functionally graded scaffolds constructed with triply periodic minimal surface, *Additive Manuf.* 32 (2020) 101015.